Constant Modulus OTFS Based on Zak Transform of Complementary Sequences for Joint Radar and Communications

Aitor Correas-Serrano, Nikita Petrov, Maria A. Gonzalez-Huici, and Alexander Yarovoy, *Fellow, IEEE*

***Abstract*—The effect of amplifier-related signal amplitude compression in orthogonal time–frequency space (OTFS) waveform for radar and communications systems is considered. A novel approach to OTFS waveform generation is proposed, where complementary sequences are used with the Zak transform to encode delay-Doppler symbols and form an OTFS time-domain signal with a constant envelope. The high peak-to-average power ratio (PAPR) of conventional OTFS can cause amplifier saturation, leading to spectral noise and performance degradation in both communication and radar systems due to amplitude clipping. This issue can be critical in dual-function radar and communication applications, where high power may be crucial in both use cases. The proposed waveform, namely, constant modulus OTFS (CM-OTFS), offers an alternative to standard OTFS when high-power or low-cost amplification is required. The sensing and communications performances of CM-OTFS are evaluated through numerical simulations and compared with pristine and amplifier-distorted OTFS waveforms. CM-OTFS demonstrates slightly degraded sensing performance and lower communication rate than pristine OTFS but outperforms amplifier-distorted OTFS signals. The performance of CM-OTFS is evaluated through radar and communication simulations, as well as radar measurements using the waveform-agile PARSAX radar.**

***Index Terms*—Complementary sequences, dual function radar and communications (DFRC), integrated sensing and communications (ISAC), orthogonal time–frequency space (OTFS), peak-to-average power ratio (PAPR), radar sensing, Zak transform.**

I. Introduction

SOFTWARE-DEFINED radar systems capable of generating fully digital waveforms, coupled with the challenge of an increasingly congested spectrum, have increased interest in systems simultaneously performing communication and sensing tasks within the same frequency bands [1]. A variety of names are used to refer to these systems, such as dual function radar and communications (DFRC), joint communications and sensing (JCS and JCAS), and integrated radar and sensing (ISAC) systems. Various forms of ISAC functionality have been explored, such as sidelobe information embedding in radar systems [2], coexistence through array partitioning and waveform optimization [3], index modulation through exploitation of the different degrees of freedom in radar systems [4], or leveraging frame structures in the existing communication protocols to facilitate radar operations [5]. Another prevalent method for ISAC involves directly employing communication waveforms for radar, made feasible by the development of fully digital radar systems [6]. In this setting, multicarrier waveforms based on orthogonal frequency division multiplexing (OFDM) have shown promise for achieving strong radar and communication performance without requiring substantial alterations to existing communication system designs [7], [8], [9].

Orthogonal time–frequency spacing (OTFS) [10] is a good alternative to OFDM for communications in high-mobility scenarios and is an increasingly popular candidate for joint sensing and communication systems [11]. OTFS shows improved robustness to Doppler shifts in comparison with OFDM in communications applications [12], [13]. At the same time, the radar performance of both waveforms is comparable [14], [15] and is primarily dependent on the complexity of the chosen radar receiver architecture [16]. Moreover, OTFS has shown comparable flexibility in terms of time and frequency usage to accommodate multiple communication users or radar transmitters and avoid interference in both the time–frequency [17], [18], [19] and spatial [20] domain. Another characteristic that OTFS shares with OFDM, however, is a peak-to-average power ratio (PAPR) greater than one [21], meaning that the envelope of the transmitted time-domain signal is not constant amplitude. The expected PAPR of OFDM increases with the number of subcarriers (fast-time radar samples) [22] in the transmitted signal. In contrast, in OTFS, the expected PAPR increases with the number of subsymbols [21] transmitted over slow time in one radar frame. Regardless of the different parameter dependences, a nonuniform envelope requires the use of highly linear power amplifiers in the transmitter to avoid signal distortion that would impact both radar and communication performance [23]. This issue is particularly relevant to radar and joint radar and communications applications, where high power is crucial due to the attenuation of round-trip wave propagation. Considering the potential of OTFS for ISAC applications, this is a significant drawback.

Received 19 November 2024; revised 23 February 2025 and 9 July 2025; accepted 4 August 2025. Date of publication 8 August 2025; date of current version 25 August 2025. *(Corresponding author: Aitor Correas-Serrano.)*

Aitor Correas-Serrano and Maria A. Gonzalez-Huici are with the Fraunhofer FHR, 53343 Wachtberg, Germany (e-mail: aitor.correas@fhr.fraunhofer.de; maria.gonzalez@fhr.fraunhofer.de).

Nikita Petrov is with NXP Semiconductors, 5656 AG Eindhoven, The Netherlands (e-mail: nikita.petrov@nxp.com).

Alexander Yarovoy is with the Department of Microelectronics, TU Delft, 2628 CD Delft, The Netherlands (e-mail: a.yarovoy@tudelft.nl).

Digital Object Identifier 10.1109/TRS.2025.3597095

Several approaches have been investigated to minimize the PAPR in OFDM signals. An iterative technique was proposed in [24] to reduce the PAPR, resulting in a signal spread across a greater frequency bandwidth. Convex optimization is used in [25] to design low PAPR waveforms for an ISAC base station dividing OFDM subcarriers between remote sensing and communications applications. This technique is suitable for generating signals with spectral nulls but not for real-time implementation in adaptive systems due to the high computational load. Another alternative is to use the so-called constant-envelope OFDM [26]. However, constant-envelope OFDM signaling presents several challenges related to phase-only information encoding. No similar approaches have been proposed for OTFS, although it is reasonable to assume that some of them can be adapted to the waveform, given their similarities.

In this work, we propose a method to form unit-PAPR OTFS frames based on generating complementary sequences from the information data to be transmitted. The proposed approach is inspired by the work in [27], [28], and [29], where a similar technique is applied to achieve constant-modulus OFDM (CM-OFDM). The approach in [29] is reformulated to fit the Zak transform-based implementation of OTFS, where the delay-Doppler message is directly transformed into the time-domain signal without an intermediate time–frequency representation, thereby formulating the first constant-envelope OTFS variant in the literature. We present a complete ISAC chain: waveform generation, transmitter, and radar/communications receivers within one unified framework. The aim is to satisfy the need of a communications-capable waveform that is both Doppler tolerant (unlike CM-OFDM) and constant envelope (unlike traditional OTFS). Specifically, the main contributions of this article are the following.

1) Novel constant envelope version of OTFS: We formulate constant-modulus OTFS (CM-OTFS) by adapting the complementary-sequence concept from the time–frequency domain (CM-OFDM) to the Zak-transform-based delay–Doppler domain. For each subcarrier, two complementary sequences are built from the slow-time symbols of the OTFS frame in an iterative process, resulting in a final constant-envelope time-domain signal. Double differential encoding (DDE) and decoding are used to deal with cumulative phase errors during CM-OTFS symbol recovery, as proposed for CM-OFDM in [28]. Radar and communication receivers compatible with the proposed CM-OTFS waveform are presented, completing the concept for an ISAC CM-OTFS system.
2) A simulation-based and experimental evaluation of the performance of the proposed CM-OTFS waveform for monostatic single-input-single-output single-input single-output (SISO) radar applications. The performance is compared with standard OTFS under nonlinear amplifier-induced signal distortion.
3) A simulation-based study validation of the communications performance of constant-modulus OTFS. A numerical comparison with standard OTFS under amplifier distortion is drawn using standard 3GPP vehicular channel models for simulation, and the compatibility of CM-OTFS with orthogonal multiple access in the frequency domain is tested. Furthermore, the symbol-recovery processing chain is validated experimentally.

While we focus on the single user/transmitter scenario, we explore the compatibility of CM-OTFS with known orthogonal time–frequency multiplexing approaches [17], [30]. The exploration of nonorthogonal multiple access approaches, e.g., in the beamspace [20], is beyond the scope of this work.

The remainder of this article is structured as follows. Section II presents a mathematical description of OTFS signal generation and channel effects, discusses the issue of PAPR in OTFS waveforms, and presents the CM-OTFS signal generation method. Section III includes the descriptions of the CM-OTFS radar signal model and receiver. Section IV presents the numerical radar and communications performance simulations for the proposed CM-OTFS system concept, and Section V extends these results with experimental validation for CM-OTFS radar and communications. Finally, concluding remarks are given in Section VI.

A. Notation

Throughout this article, $\mathbf{A}^H$ and $\mathbf{A}^{-1}$ denote the conjugate transpose and inverse of the matrix $\mathbf{A}$, respectively; vec($\mathbf{A}$) turns the $N \times M$ matrix $\mathbf{A}$ into an $NM \times 1$ vector $\mathbf{a}$, and $\text{vec}(\mathbf{a})^{-1}_{N\times M}$ is the inverse operation. For a vector $\mathbf{a}$, $\mathbf{a}(n)$ denotes a dependency with a parameter n, and $a[m]$ denotes its mth element. Subscripts are used to differentiate between different but related vectors (e.g., $\mathbf{c}_1$ and $\mathbf{c}_2$ denote a pair of complementary sequences). Finally, $\odot$ represents the matrix elementwise (Hadamard) product.

II. OTFS ISAC System Model

Consider a single-transmitter OTFS system transmitting a message $\mathbf{X}_{\text{DD}} \in \mathbb{C}^{N\times M}$ defined in an $N \times M$ delay-Doppler grid, with N delay bins and M Doppler bins. The number of subcarriers and subsymbols in time–frequency representation is N and M, respectively, and the communication symbols are mapped to the time–frequency domain through the inverse symplectic Fourier transform (ISFFT)

$$\mathbf{X}_{\text{TF}}[n,m] = \frac{1}{\sqrt{NM}} \sum_{k=0}^{N-1} \sum_{l=0}^{M-1} \mathbf{X}_{\text{DD}}[k,l]\, e^{j2\pi\left(\frac{nk}{N} - \frac{ml}{M}\right)} \tag{1}$$

where $[k,l]$ are the index pairs in the delay-Doppler grid, and $[n,m]$ are the index pairs in the fast-time–frequency grid. The Heisenberg transform converts the time–frequency signal into the time domain for transmission. The time-domain signal $s(t)$ is given by

$$s(t) = \sum_{n=0}^{N-1} \sum_{m=0}^{M-1} \mathbf{X}_{\text{TF}}[n,m]\, g_{tx}(t-nT)\, e^{j2\pi m\Delta f(t-nT)} \tag{2}$$

where g_{tx} is the transmit pulse. Assuming a rectangular transmit pulse and a critically sampled signal, (1) and (2) can be written in compact matrix notation as

$$\mathbf{X}_{\text{TF}} = \mathbf{F}_N \mathbf{X}_{\text{DD}} \mathbf{F}_M^H \tag{3}$$

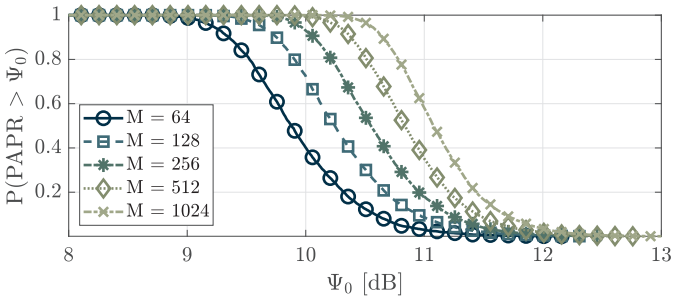

Fig. 1. Complementary cumulative distribution function (CCDF) of PAPR in OTFS signals for different values of M, numerically calculated with 5000 simulations for each data point. In all examples, $N = 256$.

and

$$\mathbf{s} = \text{vec}\left(\mathbf{F}_N^H \mathbf{X}_{\text{TF}}\right) = \text{vec}\left(\mathbf{X}_{\text{DD}} \mathbf{F}_M^H\right) \tag{4}$$

where $\mathbf{F}_N \in \mathbb{C}^{N\times N}$ and $\mathbf{F}_M \in \mathbb{C}^{M\times M}$ are the normalized Fourier transform matrices. The discrete time-domain signal $\mathbf{s} \in \mathbb{C}^{NM\times 1}$ is transformed to the analog domain with a digital-to-analog converter (DAC) before undergoing I/Q modulation and up-mixing to the desired carrier frequency f_c. Note that in (4), a single discrete Fourier transform (DFT) is used to map the delay-Doppler domain symbols to the time-domain signal. This transform is referred to as the Zak transform and allows for the synthesis of the OTFS time-domain signal without an intermediate time–frequency representation.

A. PAPR in OTFS Signals

A single DFT across the Doppler symbols is required to go from the delay-Doppler representation ($\mathbf{X}_{\text{DD}}$) to the time-domain transmitted signal $\mathbf{s}$, as shown in (4). This is the Zak transform, and it is the reason why the expected PAPR of OTFS increases with M [21]. The PAPR of a specific OTFS frame depends on the transmitted message and is, therefore, best modeled as a random variable, assuming that the probability of different messages is uniform for any given frame. The complementary cumulative probability distribution functions of the PAPR in an OTFS signal for different values of M are shown in Fig. 1, showcasing the dependency with the number of subsymbols, as well as the expected PAPR values in realistic OTFS frames for quadrature phase shift keying (QPSK) modulation. We refer the reader to [21] for a deeper study on the PAPR of OTFS with a variety symbol constellations and frame sizes.

The increase in PAPR can lead to radar performance degradation if the signal is transmitted through a saturated amplifier. Amplifier saturation is common in radar systems to maximize output power and increase target detection probability. In this work, the power amplifier is modeled as an instantaneous nonlinearity [31]. Considering as input an arbitrary complex signal

$$s_{\text{in}}(t) = A_{\text{in}}(t) \exp\left(j\phi_{\text{in}}(t)\right) \tag{5}$$

and the output

$$s_{\text{out}}(t) = G\left(A_{\text{in}}(t)\right) \exp\left(j\left(\phi_{\text{in}}(t) + \Phi\left(A_{\text{in}}(t)\right)\right)\right) \tag{6}$$

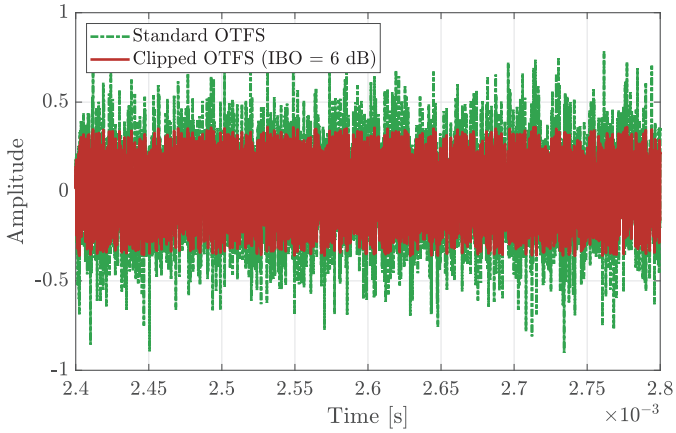

Fig. 2. Real part of a standard OTFS signal, and the same signal with amplifier-related amplitude clipping.

where G and Φ are the input-amplitude-dependent distortions of the amplitude (clipping) and phase of the output signal, respectively. We use the model from [26], [32]

$$G\left(A_{\text{in}}(t)\right) = \frac{g_0 A_{\text{in}}(t)}{1 + \left(A_{\text{in}}(t)/A_{\text{sat,in}}\right)^2} \tag{7}$$

$$\Phi\left(A_{\text{in}}(t)\right) = \frac{\alpha_\phi A_{\text{in}}^2(t)}{1 + \beta_\phi A_{\text{in}}^2(t)} \tag{8}$$

which is parametrized by the gain g_0, the input saturation amplitude $A_{\text{sat,in}}$, and the amplitude-dependent phase modulation α_ϕ and β_ϕ, which we set to $\alpha_\phi = \pi/6$ and $\beta_\phi = 0.2$. Finally, amplitude clipping is defined by the value of $A_{sat,in}$, which is set by the PAPR of the signal and the input power backoff (IBO) [33], defined as

$$\text{IBO} := \frac{A_{\text{sat,in}}}{\mathbb{E}\left(A_{\text{in}}^2(t)\right)} \geq 1. \tag{9}$$

For any constant envelope signal, such as the CM-OTFS presented in this work, IBO = 0 dB. The lower the value of IBO for a nonconstant envelope signal, the stronger the amplitude clipping in the output signal. The effect of amplitude clipping in the time-domain signal is depicted in Fig. 2. The integrated and peak sidelobe levels in the radar range-Doppler estimation for different levels of amplifier distortion (parametrized with the IBO) are shown in Fig. 3, where a loss of almost 10 dB in dynamic range occurs for low IBO values. The envelope variation of time-domain OTFS arises from the Doppler domain symbol integration through the Zak transform, and it can lead to the distortion shown in Fig. 2 sidelobe level increase shown in Fig. 3. However, it is possible to use the Zak transform to formulate a constant-modulus version of OTFS signals using complementary sequences generated from the transmitted symbols in the Doppler domain.

B. Constant Modulus OTFS

Let us consider the same delay-Doppler message $\mathbf{X}_{\text{DD}} \in \mathbb{C}^{N\times M}$ from Section II as formed by N data vectors $\mathbf{a}(n) \in \mathbb{C}^{1\times M}$ $\forall\, n \in [1, N]$, such that

$$\mathbf{X}_{\text{DD}} = \left[\mathbf{a}(1)^T, \mathbf{a}(2)^T, \ldots, \mathbf{a}(N)^T\right]^T. \tag{10}$$

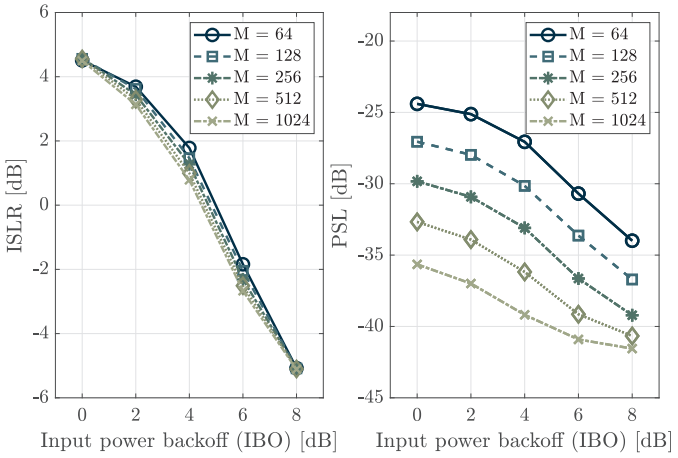

Fig. 3. Integrated and peak sidelobe levels of a range-Doppler estimation in a distorted OTFS frame for different values of M and IBO. Lower values of IBO represent a higher degree of amplitude distortion.

A pair of complementary sequences $\mathbf{c}_1$ and $\mathbf{c}_2$ are built from each data vector $\mathbf{a}(n) \in \mathbb{C}^{1\times M}$, where n denotes the delay index in the delay-Doppler representation of the OTFS signal. The sequence pair $\mathbf{c}_1$ and $\mathbf{c}_2$ are complementary when the sum of their autocorrelations $\mathbf{r}_{11}$ and $\mathbf{r}_{22}$ adds up to a δ function

$$\mathbf{r}_{11} + \mathbf{r}_{22} \propto \delta\left[\eta\right]. \tag{11}$$

Algorithm 1 CM-OTFS Complementary Sequence Generation

Input: Data vectors $\mathbf{a}(n)$, M Doppler bins, N delay bins, coupling parameter r
Output: Complementary sequences $\mathbf{c}_1^{(M)}$, $\mathbf{c}_2^{(M)}$
begin
Initialization: $\mathbf{c}_1^{(-1)} := [1, 1]$, $\mathbf{c}_2^{(-1)} := [1, -1]$ (See Eq. (12))
Compute normalization factor $\alpha = 1/\sqrt{\mathbb{E}[\|\mathbf{a}\|^2] + r^2}$
for $n = 1$ to N **do**
  for $m = 0$ to $M - 1$ **do**
    1. Compute unitary transform matrix:
    Define $\mathbf{S}_m$ as in Eq. (13)
    2. Expand complementary sequences:
    Update $\mathbf{c}_1^{(m)}$, $\mathbf{c}_2^{(m)}$ as in Eq. (14)
  end for
  3. Form $\mathbf{d}_1(n)$, $\mathbf{d}_2(n)$ as in Eq. (15), (16)
end for
end

Following Algorithm 1, an initial pair of Golay sequences $\mathbf{c}_1^{(-1)}$ and $\mathbf{c}_2^{(-1)}$ are iteratively extended into longer sequences through 2×2 unitary transforms using the data symbols contained in $\mathbf{a}(n)$. Let us define the initial sequences as

$$\mathbf{c}_1^{(-1)} := [1, 1], \quad \mathbf{c}_2^{(-1)} := [1, -1]. \tag{12}$$

For the data vector $\mathbf{a}(n)$ associated with a specific subcarrier n, this sequence is extended by one symbol at a time through an M-long iterative process of unitary transforms defined as

$$\mathbf{S}_m = \alpha \begin{bmatrix} a[m] & -r \\ r & a^*[m] \end{bmatrix} \tag{13}$$

where $a[m]$ is the mth symbol from the data vector $\mathbf{a}(n)$, r is a free parameter that determines coupling between the complementary sequences, and $\alpha = 1/(\mathbb{E}[\|\mathbf{a}\|^2] + r^2)^{1/2}$ is a normalization factor. Note that we drop writing explicitly the dependency with n for compactness and clarity. In CM-OFDM, the value of r has been shown to impact communication and radar performance in opposing ways, making it a tradeoff parameter [29]. The influence of the r-value in CM-OTFS will be analyzed in Section IV.

The transforms are used to expand the pair of complementary sequences iteratively

$$\begin{bmatrix} \mathbf{c}_1^{(m)} \\ \mathbf{c}_2^{(m)} \end{bmatrix} = \mathbf{S}_m \begin{bmatrix} \mathbf{c}_1^{(m-1)} & 0 \\ 0 & \mathbf{c}_2^{(m-1)} \end{bmatrix} \tag{14}$$

which generates two complementary sequences $\{\mathbf{c}_1^{(m)}$ and $\mathbf{c}_2^{(m)}\}$. The iterative sequence expansion in (14) results in two expanded sequences $\{\mathbf{c}_1, \mathbf{c}_2\} \in \mathbb{C}^{1\times M'}$, where we use $M' := M + 2$ for compactness of notation. Mirroring the steps in [34] for CM-OFDM, the resulting sequences are interleaved to form a new pair of complementary sequences $\mathbf{d}_1$, $\mathbf{d}_2 \in \mathbb{C}^{1\times 2M'}$

$$\mathbf{d}_1 = [c_1[0], c_2[0], c_1[1], c_2[1], \ldots, c_2[M+1]] \tag{15}$$
$$\mathbf{d}_2 = [c_1[0], -c_2[0], c_1[1], -c_2[1], \ldots, -c_2[M+1]] \tag{16}$$

that will be used to assemble the OTFS time signal with the Zak transform. For N delay bins, the process in (13)–(16) is repeated for each vector $\mathbf{a}(n)$, resulting in N pair of sequences, indexed as $\{\mathbf{d}_1(n), \mathbf{d}_2(n)\}\ \forall\ n \in [1, N]$. Two new delay-Doppler signals composed of these complementary sequences can be written as

$$\hat{\mathbf{X}}_{\mathrm{DD}_1} = \left[\mathbf{d}_1(1)^T, \mathbf{d}_1(2)^T, \ldots, \mathbf{d}_1(N)^T\right]^T \tag{17}$$
$$\hat{\mathbf{X}}_{\mathrm{DD}_2} = \left[\mathbf{d}_2(1)^T, \mathbf{d}_2(2)^T, \ldots, \mathbf{d}_2(N)^T\right]^T \tag{18}$$

and finally, two intermediate time-domain signals can be generated as in (4) with the Zak transform

$$\mathbf{z}_1 = \mathrm{vec}\left(\hat{\mathbf{X}}_{\mathrm{DD}_1}\mathbf{F}_{\mathrm{M}}^{\mathrm{H}}\right) \tag{19}$$
$$\mathbf{z}_2 = \mathrm{vec}\left(\hat{\mathbf{X}}_{\mathrm{DD}_2}\mathbf{F}_{\mathrm{M}}^{\mathrm{H}}\right) \tag{20}$$

where each $\mathbf{z}_1$ and $\mathbf{z}_2$ are the OTFS subsignals of length $2NM'$, and are used to construct the final OTFS constant-modulus time-domain signals

$$\hat{\mathbf{s}}_1 = \mathbf{z}_1 + j\exp\left(j\boldsymbol{\phi}_c\right) \odot \mathbf{z}_2 \tag{21}$$
$$\hat{\mathbf{s}}_2 = \mathbf{z}_1 - j\exp\left(j\boldsymbol{\phi}_c\right) \odot \mathbf{z}_2 \tag{22}$$

where $\{\hat{\mathbf{s}}_1, \hat{\mathbf{s}}_2\} \in \mathbb{C}^{1\times 2M'}$, and $\boldsymbol{\phi}_c = \angle\mathbf{z}_1 - \angle\mathbf{z}_2 \in \mathbb{R}^{1\times 2M'}$. In (21) and (22), the phase of $\mathbf{z}_2$ is replaced with the phase of $\mathbf{z}_1$ and placed in quadrature, which results in a constant modulus OTFS (CM-OTFS) time-domain signal. Signals $\hat{\mathbf{s}}_1$ and $\hat{\mathbf{s}}_2$ are both transmitted (e.g., in consecutive delay bins or as double-length Doppler messages) to use differential decoding to avoid errors in the process of recovering the data vectors $\mathbf{a}(n)$. This reflects the main tradeoff of both CM-OFDM and the proposed CM-OTFS when using this constant-modulus formulation: $4M$ total symbols are transmitted to encode a total of M data symbols, reducing the efficiency by a factor of four.

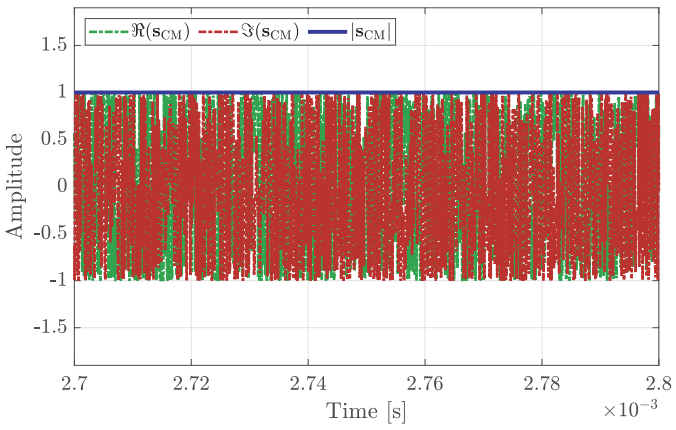

Fig. 4. Real and imaginary part resulting from the CM-OTFS process, using the same data symbols as in the signal depicted in Fig. 2. The amplitude of the signal (blue curve) is constant.

The process generates two complementary sequences from the communication symbols and uses the Zak transform to synthesize the OTFS time-domain signal, replacing the operation in (4). For N delay indexes of the original $\mathbf{X}_{DD}$ data matrix, the resulting time-domain signal is

$$\mathbf{s}_{CM} = \text{vec}\left(\mathbf{S}_{CM}\right) \tag{23}$$

where $\mathbf{S}_{CM} \in \mathbb{C}^{2N\times 2M}$ is defined as

$$\mathbf{S}_{CM} = \left[\hat{\mathbf{s}}_1^T(n=1), \hat{\mathbf{s}}_2^T(n=1), \ldots, \hat{\mathbf{s}}_1^T(n=N), \hat{\mathbf{s}}_2^T(n=N)\right]^T \tag{24}$$

which has a constant envelope, as shown in Fig. 4, and encodes $N \times M$ communications symbols in a $2N \times 2M'$ frame.

Before moving forward, it is worth discussing some already apparent drawbacks. First, there is a reduction in spectral efficiency, as a frame of size $4NM'$ is used to encode NM QPSK delay-Doppler symbols, which corresponds to a reduction by a factor of four. Moreover, this approach to generate a constant-modulus signal has only been defined for communication dictionaries without amplitude modulation, restricting this approach to phase-only dictionaries [34], such as the QPSK used for this work.

Algorithm 2 CM-OFTS Delay-Doppler Symbol Recovery

Input: $\hat{\mathbf{Y}}_{DD_1}, \hat{\mathbf{Y}}_{DD_2}, r, M, N, \hat{\mathbf{c}}_1^{(0)}, \hat{\mathbf{c}}_2^{(0)}$
Output: $\hat{\mathbf{a}}(n) \in \mathbb{C}^{1\times M} \quad \forall n \in [1, N]$
begin
Initialization: $\hat{\mathbf{a}}(n) = \mathbf{0} \quad \forall n \in [1, N]$;
for $n = 1$ to N **do**
  for $m = 0$ to $M-1$ **do**
    1. Calculate $\hat{\mathbf{a}}(n)_{M-m}$ **data symbol** (30);
    2. Update complementary sequences:
    $\mathbf{c}_1^{(m+1)}$ from $\hat{a}[M-m]$ and $\mathbf{c}_1^{(m)}$ (31);
    $\mathbf{c}_2^{(m+1)}$ from $\hat{a}[M-m]$ and $\mathbf{c}_2^{(m)}$ (32);
  end for
end for
end

To recover the delay-Doppler symbols $\mathbf{a}(n)$, the previous process is undone. Let us assume a received signal $\mathbf{r}_{CM} \in \mathbb{C}^{4NM'\times 1}$ after channel compensation

$$\mathbf{r}_{CM} = \mathbf{s}_{CM} + \mathbf{w} \tag{25}$$

where $\mathbf{w}$ is the additive white Gaussian noise (AWGN). If we consider $\mathbf{R}_{CM} = \text{vec}(\mathbf{r}_{CM})^{-1}_{2N\times 2M'}$, then $\{\hat{\mathbf{s}}_1(n), \hat{\mathbf{s}}_2(n)\}$ can be recovered by selecting the odd and even rows of $\mathbf{R}_{CM}$, respectively, undoing the interleaving in (24). After some simple algebra, we can find that

$$\hat{\mathbf{z}}_1 = \frac{\hat{\mathbf{s}}_1 + \hat{\mathbf{s}}_2}{2} \tag{26}$$

$$\hat{\mathbf{z}}_2 = \exp\left(-j\phi_c\right)\frac{\hat{\mathbf{s}}_1 - \hat{\mathbf{s}}_2}{2j} \tag{27}$$

with which we calculate the delay-Doppler representation of the received signal

$$\hat{\mathbf{Y}}_{DD_1} = \text{vec}^{-1}_{N\times 2(M+2)}\left(\hat{\mathbf{z}}_1\right)\mathbf{F}_{2M'} \tag{28}$$

$$\hat{\mathbf{Y}}_{DD_2} = \text{vec}^{-1}_{N\times 2(M+2)}\left(\hat{\mathbf{z}}_2\right)\mathbf{F}_{2M'} \tag{29}$$

from which we can get the estimate of the sequences $\hat{\mathbf{d}}_1$, $\hat{\mathbf{d}}_2$, and $\hat{\mathbf{c}}_1$, $\hat{\mathbf{c}}_1$ by undoing the steps in (15)–(18). Finally, from the complementary pairs $\hat{\mathbf{c}}_1$, $\hat{\mathbf{c}}_1$, the original symbols are extracted in an iterative manner that reverses the steps in (14), and for each $m \in \{0, \ldots, M-1\}$, as shown in Algorithm 2, where the estimation of the transmitted symbols is given by

$$\hat{a}\left[M-m\right] = r\frac{\hat{c}_1^{(m)}[1] - \hat{c}_2^{(m)*}[M-m]}{\hat{c}_2^{(m)}[1] + \hat{c}_1^{(m)*}[M-m]} \tag{30}$$

and $\{\mathbf{c}_1^{(m+1)}, \mathbf{c}_2^{(m+1)}\}$ for the next iteration are given by the inversion of (14) using the conjugate transpose of the Hermitian matrix $\mathbf{S}_m$

$$\mathbf{c}_1^{(m+1)} = \hat{a}\left[M-m\right]\hat{\mathbf{c}}_1^{(m)} + r\hat{\mathbf{c}}_2^{(m)} \tag{31}$$

$$\mathbf{c}_2^{(m+1)} = -r\hat{\mathbf{c}}_1^{(m)} + \hat{a}\left[M-m\right]\hat{\mathbf{c}}_2^{(m)} \tag{32}$$

where in each step a new data symbol $\hat{a}[M-m]$ is recovered, and the sequences $\mathbf{c}_1^{(m+1)}$ and $\mathbf{c}_2^{(m+1)}$ have one less length than their predecessors, as their last and first elements, respectively, are zero. Note that the calculation of the sequences $\{\mathbf{c}_1^{(m+1)}, \mathbf{c}_2^{(m+1)}\}$ is performed for each n, but the index is dropped for compactness. This process is repeated for each $n \in \{1, \ldots, N\}$, thus recovering all n data vectors $\hat{\mathbf{a}}(n)$, that forms our received delay-Doppler data matrix

$$\hat{\mathbf{X}}_{DD} = \left[\hat{\mathbf{a}}(1)^T, \hat{\mathbf{a}}(2)^T, \ldots, \hat{\mathbf{a}}(N)^T\right]^T. \tag{33}$$

III. CM-OTFS Radar

The discrete constant-modulus time-domain signal $\mathbf{s}_{CM}$ is transformed to the analog domain with a DAC before being modulated to the desired carrier frequency and transmitted. Assuming co-located radar operation, the received signal after illuminating a scene with K targets characterized by a path delay τ and a Doppler shift f_d can be written as

$$r(t) = \sum_{k=1}^{K}\alpha_k s_{CM}(t-\tau_k)\exp\left(j2\pi f_{d,k}t\right) + w \tag{34}$$

where $s_{\mathrm{CM}}(t)$ is the transmitted time-domain signal, α_k is the complex amplitude associated with the kth target, and w is AWGN. The delay and Doppler effects in the signal can be represented in the time–frequency domain compactly by using the generalized multicarrier radar signal model [35]. The time–frequency representation $\mathbf{Y}_{\mathrm{TF}} \in \mathbb{C}^{2N\times 2M}$ of the critically sampled received time-domain signal $\mathbf{r}$ is given by

$$\mathbf{Y}_{\mathrm{TF}} = \mathbf{F}_{2\mathrm{N}}\mathrm{vec}^{-1}_{2N\times 2M'}(\mathbf{r}) \tag{35}$$

and the radar delay-Doppler effects in the time–frequency signal for each target can be written as

$$\mathbf{r} = \mu\psi\mathrm{vec}\left(\mathbf{\Gamma_1}\mathbf{F}_{\mathrm{N}}^{\mathbf{H}}\mathbf{A}\mathbf{X}_{\mathrm{TF}}\mathbf{\Gamma_2}\right) \tag{36}$$

where, for a delay τ and a Doppler shift f_d, the following constants are defined:

$$\gamma = \exp\left(-j2\pi\frac{T}{N}f_d\right) \tag{37}$$

$$a = \exp\left(-j2\pi\Delta f\tau\right) \tag{38}$$

and used to build diagonal matrices modeling the time and frequency shift in the received signal

$$\mathbf{\Gamma}_1 = \mathrm{diag}\left\{\gamma^0, \gamma^1, \ldots, \gamma^{(N-1)}\right\} \tag{39}$$

$$\mathbf{\Gamma}_2 = \mathrm{diag}\left\{\gamma^0, \gamma^N, \ldots, \gamma^{(M-1)N}\right\} \tag{40}$$

where $\mathbf{\Gamma}_1 \in \mathbb{C}^{N\times N}$ represents the Doppler phase shift along subcarriers—the intercarrier interference—and $\mathbf{\Gamma}_2 \in \mathbb{C}^{M\times M}$ is the Doppler phase shift across subpulses. Analogously, a matrix form of the target range-related subcarrier phase shift is defined as

$$\mathbf{A} = \mathrm{diag}\left\{a^0, a^1, \ldots, a^{N-1}\right\} \tag{41}$$

with $\mathbf{A} \in \mathbb{C}^{N\times N}$. Finally, μ is a complex amplitude, and ψ represents the delay-dependent phase shift at carrier frequency

$$\psi = \exp\left(-j2\pi f_c\tau\right) \tag{42}$$

A radar receiver based on the time–frequency-domain phase normalization of the received signal is used to estimate the range-Doppler parameters in the received signal. This receiver assumes uncoupled range-Doppler estimation parameters, which are estimated sequentially and result in a computational complexity of $\mathcal{O}(N+M)$. The tradeoff of this assumption is a reduced Doppler tolerance and unambiguous range-Doppler estimation compared to joint delay-Doppler receivers [16]. However, the computational complexity of joint delay-Doppler receivers is $\mathcal{O}(NM)$, which makes them impractical for relatively big frame sizes and fractional time and frequency shifts. Implementing this phase-normalization-based receiver involves a pointwise multiplication to normalize the phase, followed by a symplectic finite Fourier transform (SFFT). The phase normalization is given by

$$\mathbf{Y}_{\mathrm{norm}}[n,m] = \mathbf{Y}_{\mathrm{TF}}[n,m]\exp\left(-j\Psi[n,m]\right) \tag{43}$$

where

$$\Psi[n,m] = \angle\left(\mathbf{X}_{\mathrm{TF}}[n,m]\right) \tag{44}$$

for every $n \in \{1,\ldots,2N\}$ and $m \in \{1,\ldots,2M\}$. After phase normalization, the SFFT is performed to calculate the range-Doppler map. This receiver normalizes the received signal in the time–frequency domain and transforms the result into the delay-Doppler domain. If $[\tau_k, f_{d,k}] = [0,0]$, then $\mathbf{Y}_{\mathrm{norm}}$ is an all-ones matrix, and its delay-Doppler representation $\mathbf{Y}^{\mathrm{DD}}_{\mathrm{norm}}$ appears as a peak at $[0,0]$. For any other pairs of $[\tau_k, f_{d,k}]$, the peak in $\mathbf{Y}^{\mathrm{DD}}_{\mathrm{norm}}$ is displaced to the corresponding index in the delay-Doppler plane. A block diagram of the proposed system architecture with a branching radar and communication receiver structure is shown in Fig. 5. The communication receiver follows the decoding steps presented in Section II.

TABLE I
OTFS SIMULATION WAVEFORM PARAMETERS

Parameter	Symbol	Value
Number of delay bins	N	256
Number of Doppler bins	M	256
Bandwidth	B	10 MHz
Carrier frequency	f_c	24 GHz
Symbol duration	T	25.6 μs
Intercarrier separation	Δf	39 kHz
Cyclic prefix duration	T_{cp}	12.8 μs
Communication Modulation	$(-)$	QPSK

IV. PERFORMANCE ASSESSMENT OF CONSTANT-MODULUS OTFS

In this section, numerical simulations are performed to test the performance of CM-OTFS for radar and communications. The waveform parameters in Table I are used for both radar and communications simulations.

A. CM-OTFS Radar Performance Evaluation

The performance of CM-OTFS in radar applications is tested through numerical simulations. As OTFS is particularly well suited to high-mobility applications, a carrier frequency of 24 GHz is chosen, as bands around this frequency have been used for automotive radar and are projected to be used in millimeter-wave communications for 6G under the label of frequency range 3 (FR3), therefore showing potential in applications for both sensing and communication in high-mobility scenarios [36]. The simulations are performed assuming a monostatic system, and the main waveform parameters are shown in Table I. For the scope of this work, a monostatic SISO radar is considered.

The approach followed to evaluate CM-OTFS radar performance is to compare with two References: first, a baseline standard OTFS approach with the same subcarriers (N) and subsymbols (M), and second, an OTFS waveform with amplifier-related distortion due to the nonuniform amplitude of the time-domain signal. The radar estimation is performed with the standard DFT-based spectral division receiver for all three cases. In the case of the distorted OTFS signal, the original transmitted OTFS signal is used for radar processing. Fig. 6 shows the range-velocity maps of standard OTFS, amplitude-clipped OTFS due to amplifier saturation, and CM-OTFS. Four-point targets are present in the simulation, and no tapering is used in the estimation, resulting in similar sinc-like sidelobes around the targets. A stronger noise-like background appears in the clipped-OTFS waveform when compared to

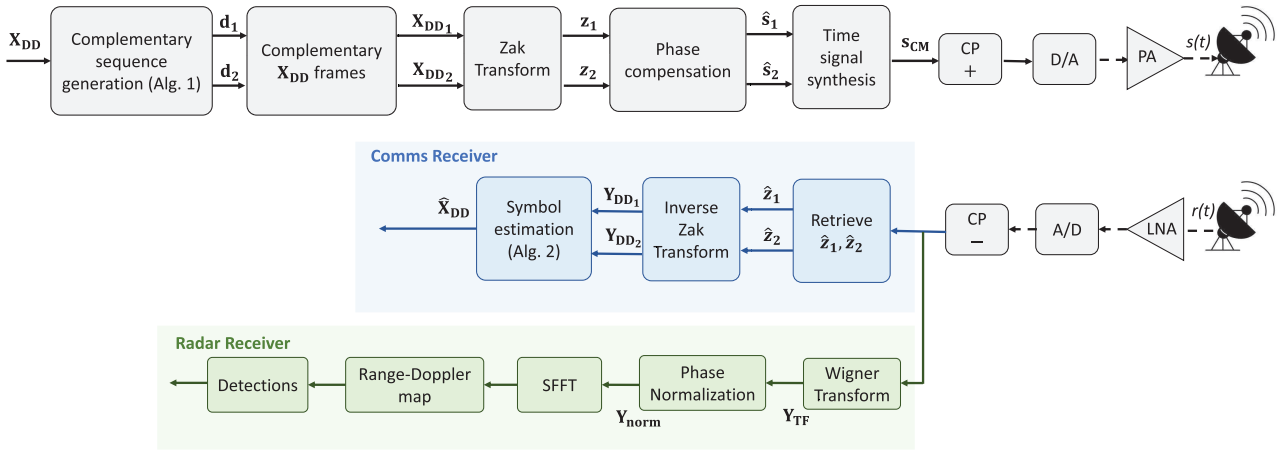

Fig. 5. Block diagram of an exemplary CM-OTFS ISAC system with dual function waveform transmission. A separate radar and communication digital signal processing chain enables using the complete waveform for both functions. The radar function relies on time–frequency processing, while the communications branch relies on the Zak transform for symbol recovery.

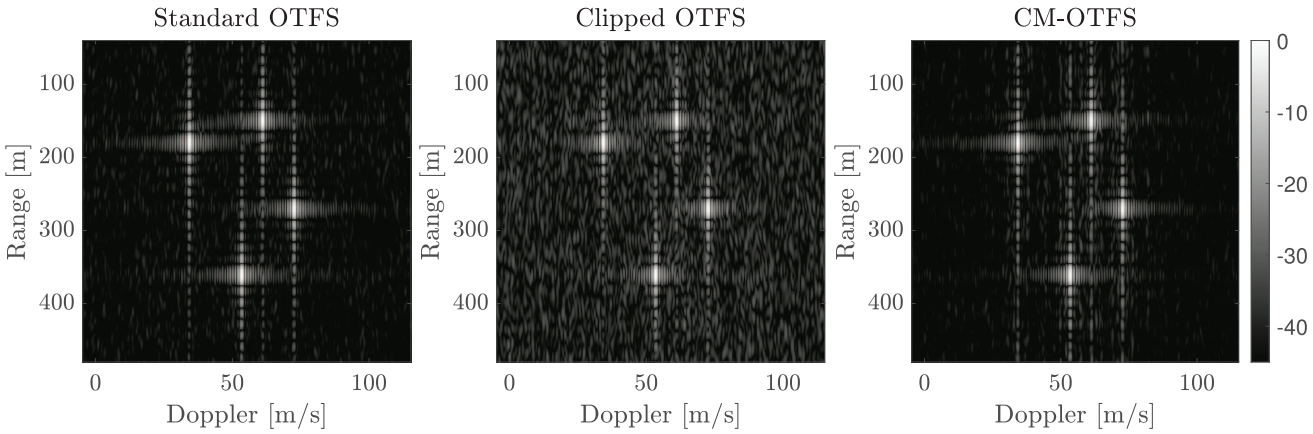

Fig. 6. Noiseless range-Doppler slice section for OTFS radar with different waveforms. On the left, standard OTFS with no amplifier effect. On the center, the same waveform with amplifier-caused amplitude clipping (IBO = 6 dB). On the right is a CM-OTFS waveform.

standard OTFS, which we attribute to the mismatch between the original signal and the distorted transmitted signal. CM-OTFS shows slightly increased noise-like sidelobes around the main range sinc-like sidelobes, but they are contained to the Doppler cells around the target. Overall, the sidelobe level of CM-OTFS is better than that of the clipped OTFS waveform and close to the performance of a standard OTFS frame.

A quantitative study of the sidelobe characteristics of the waveforms for a single target is shown in Figs. 7 and 8. Fig. 7 shows the integrated sidelobe ratio (ISLR) in the range cut, Doppler cut, and whole range-Doppler surfaces for standard OTFS and CM-OTFS for different values of r. The ISLR is defined as the integrated sidelobe power in an estimation normalized to the main-lobe peak [37]. First, when the measurement is noise-dominated (i.e., the sidelobes are buried under the noise), standard OTFS and CM-OTFS perform the same regarding sidelobe power. For sidelobe-dominated estimations, i.e., higher signal-to-noise ratio (SNR), we observe that the ISLR in the range cut increases (meaning higher sidelobe power) in CM-OTFS compared to standard OTFS. Moreover, the higher the value of the parameter r, the higher the sidelobes in the range cut. In the Doppler cut, we see a similar behavior regarding the noise, but now standard OTFS shows slightly higher sidelobe power at high noise levels. Finally, the ISLR on the range-Doppler slice shows that standard OTFS and CM-OTFS have the same sidelobe power. This implies that the differences in ISLR in the range and Doppler cuts are due to a redistribution of the sidelobe power and not an overall increase in the sidelobe level.

The changes in the structure of the sidelobes can result in increased peak-to-sidelobe level (PSL), which increases the chances of target masking. Fig. 8 shows the PSL of standard OTFS and CM-OTFS for different values of SNR. Similarly, as with ISLR, we can see that as long as the measurements are noise-dominated, the PSL of the estimation is the same in all waveforms, as it simply reflects the peak of the noise floor. For higher SNR values, we observe an increase in PSL in the range domain that worsens as the value of r decreases. Moreover, this increased range sidelobe becomes the dominating sidelobe in the entire range-Doppler domain, as shown by the fact that the PSL value in the range-Doppler surface matches the PSL value in the range cut. Another metric of interest is the error in the range and speed parameter estimation. We measure it through the mean-square error (mse) of the estimation in range and Doppler separately for the same single-target scenarios as before. The results shown in Fig. 9 indicate that CM-OTFS offers the same accuracy

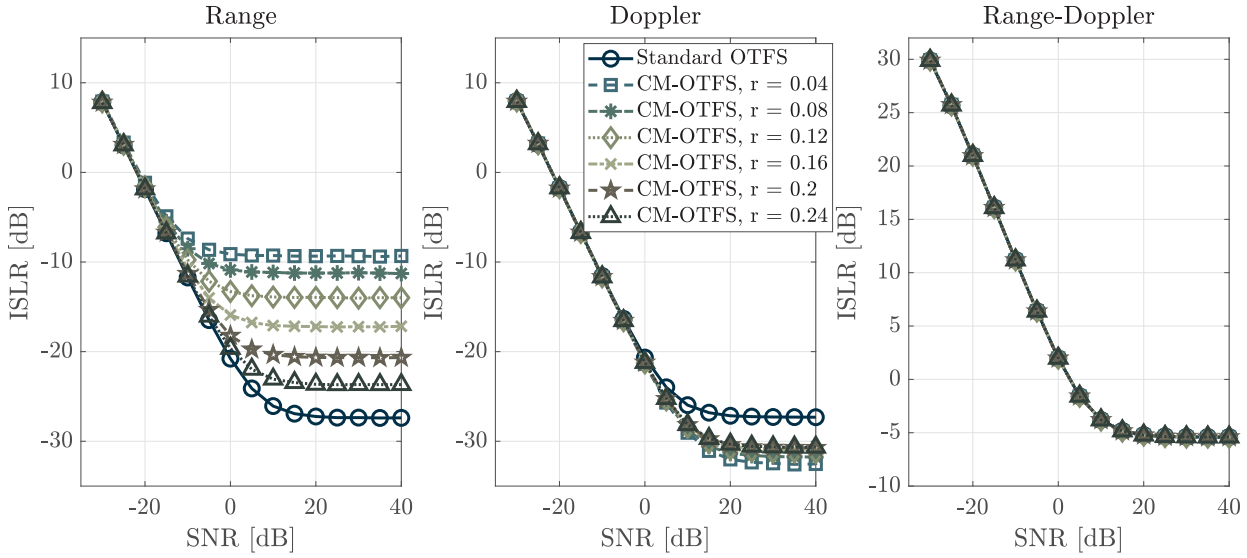

Fig. 7. Integrated sidelobe level after range-Doppler estimation in target range slice, Doppler slice, and range-Doppler map in the left, center, and right, respectively.

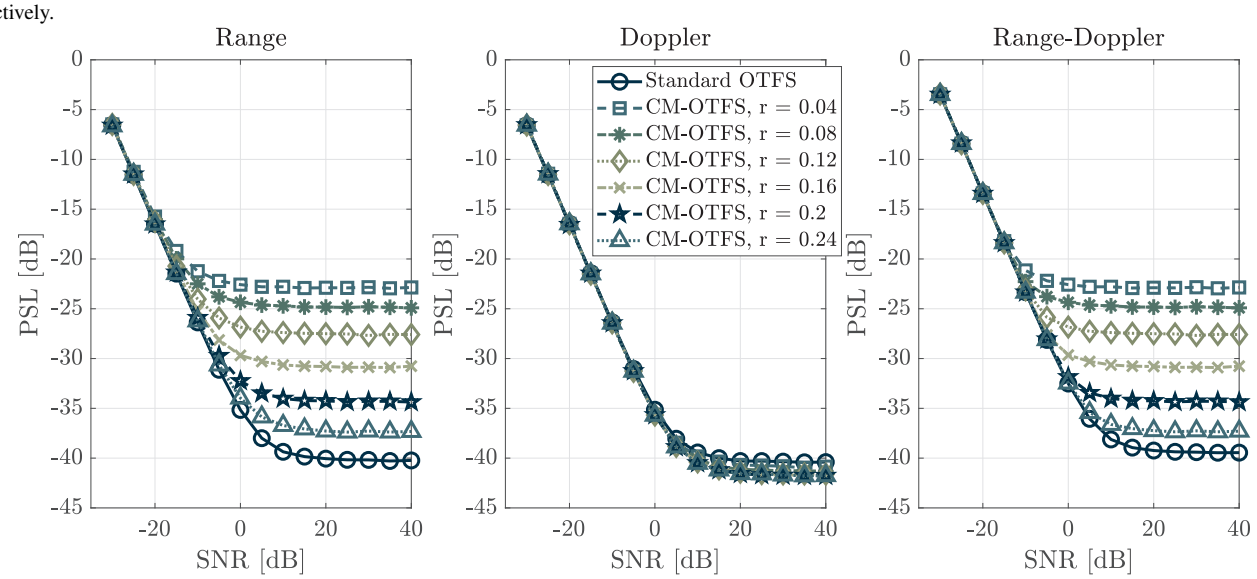

Fig. 8. Normalized peak sidelobe level after range-Doppler estimation in target range slice, Doppler slice, and range-Doppler map in the left, center, and right, respectively.

in terms of parameter estimation as pristine OTFS for single target scenarios and standard radar processing.

Overall, if we compare the results of ISLR with the ISLR in standard OTFS with amplifier clipping (Fig. 3), we can see that for a value of, e.g., IBO = 0, the expected ISLR for clipped OTFS with $M = 256$ is around 5 dB, whereas in CM-OTFS, the ISLR would be -5 dB, meaning an improvement of 10 dB over the amplifier clipped waveform, at the cost of the sidelobe-power being focused in a higher range peak sidelobe. In the end, whether a constant modulus approach is desirable in terms of radar will depend mostly on the characteristics of the amplifier and power requirements, which will define the expected distortion on the transmitted signal.

B. CM-OTFS Communication Performance Evaluation

To evaluate the communications performance of the proposed CM-OTFS waveform, a linear minimum-mean-square-error (LMMSE) detector [38] is used for an OTFS frame. It is assumed that perfect channel state information is available, the channel effects have been compensated for, and only noise is present. The goal of this evaluation is to verify that the original delay-Doppler symbols can be reconstructed from a CM-OTFS frame and, similar to the radar numerical evaluation, determine how the performance of CM-OTFS compares in comparison to a pristine OTFS frame and OTFS frames that are distorted due to the amplitude clipping caused by amplifier saturation. The same waveform parameters used in the radar simulations (Table I) are used for the simulations in this section, and the steps in (25)–(32) are followed for symbol recovery. As the number of subcarriers and subsymbols (delay and Doppler bins) is equal in both standard OTFS and CM-OTFS, CM-OTFS carries a quarter of the symbols and achieves a quarter of the communication rate. The communication symbols are sampled from a uniform random distribution.

The iterative decoding process to retrieve the data symbols from the complementary sequences in the received signal can

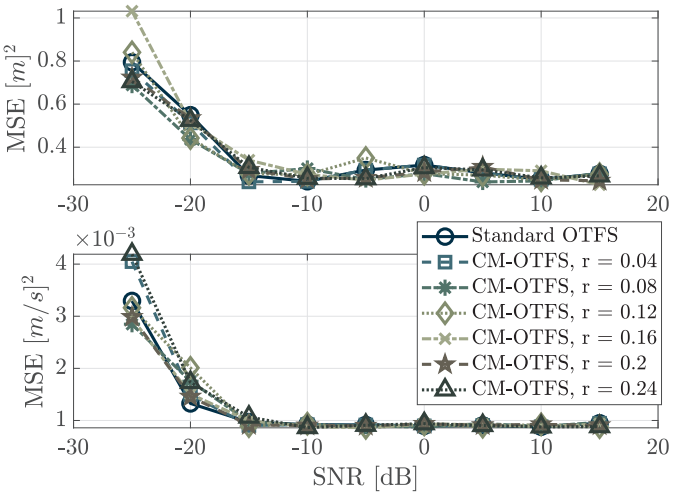

Fig. 9. Mean-squared error of the single-target radar estimation for range and speed target parameters on the top and bottom, respectively.

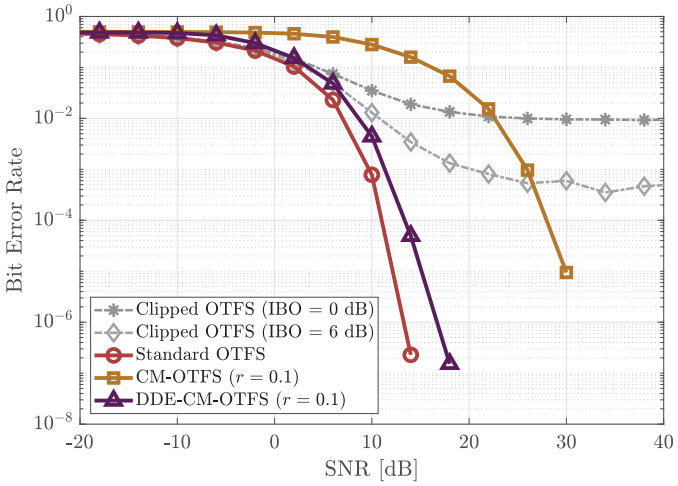

Fig. 10. BER for an increasing value of SNR for distorted and pristine OTFS and CM-OTFS with and without DDE.

result in a cumulative phase error in the presence of noise. Using a DDE in the transmitted symbols can help mitigate this effect [28]. First, the transmitted symbols $\mathbf{a}(n) \in \mathbb{C}^{1\times M}$ are separated in two subsignals formed by the even and odd Doppler indexes, $\mathbf{a}_E(n) \in \mathbb{C}^{1\times M/2}$ and $\mathbf{a}_O(n) \in \mathbb{C}^{1\times M/2}$, respectively. Assuming a phase-only modulation, differential encoding can be applied to each of them separately, resulting in

$$d_E[m] = a_E[m]\, a_E[m-1] \tag{45}$$

$$d_O[m] = a_O[m]\, a_O[m-1] \tag{46}$$

and then, new data vectors $\mathbf{a}^{\mathrm{DDE}} \in \mathbb{C}^{1\times M}$ can be formed by interleaving the elements of $\mathbf{d}_O$ and $\mathbf{d}_E$. Double differential decoding is applied at the receiver by reversing the previous process. For consistency with (45) and (46), we relabel the recovered differential-encoded symbols from (30) as $\hat{\mathbf{a}}^{\mathrm{DDE}}$, which we separate in even $\hat{\mathbf{d}}_E$ and odd $\hat{\mathbf{d}}_O$ and used to compute the double differential decoding

$$\hat{a}_E[m] = \hat{d}_E[m] \exp\left(-j \arg\left(d_E[m]\right)\right) \tag{47}$$

$$\hat{a}_O[m] = \hat{d}_O[m] \exp\left(-j \arg\left(d_O[m]\right)\right) \tag{48}$$

and the recovered data vectors $\hat{\mathbf{a}}^{\mathrm{DDE}} \in \mathbb{C}^{1\times M}$ are formed by interleaving the elements of $\hat{\mathbf{a}}_O$ and $\hat{\mathbf{a}}_E$ for each $n \in \{0, \ldots, N-1\}$. In (47) and (48), the phase of the previous symbol is used for differential decoding to avoid any changes in amplitude. This process is repeated for each $n \in \{0, \ldots, N-1\}$, resulting in the estimated vectors $\hat{\mathbf{a}}^{\mathrm{DDE}}(n)$ that form the estimated delay-Doppler data matrix as in (33). Note that to perform DDE, the transmitter and receiver need to agree on a starting reference phase for the first symbol, which, in our case, is 0Â°. We label the resulting signal double differential encoded CM-OTFS (DDE-CM-OTFS).

The bit error rate (BER) for the evaluated waveforms and increasing SNR values is shown in Fig. 10. The results are the average of 1000 Monte Carlo simulations for each waveform and SNR step. The simulations show that undistorted OTFS (red) achieves the best BER values, achieving the same BER as CM-OTFS (yellow), with SNR being lower by 15 dB. Although both CM-OTFS and undistorted OTFS tend toward a BER of zero for sufficiently high values of SNR, an SNR loss of around 15 dB is severe in most applications, even if the constant-envelope property of CM-OTFS enables high-power transmission. The decrease in BER for a given SNR is caused by the iterative nature of the symbol retrieval from the complementary sequences, as an early error propagates to future iterations, as seen in CM-OFDM. DDE [34] can be used prior to the complementary sequence synthesis to ensure the phase errors only propagate for a maximum of two iterations in the decoding process. The resulting waveform, namely, DDE-CM-OTFS, significantly improves the performance of CM-OTFS and achieves BER similar to standard pristine OTFS, as shown in Fig. 10 (purple curve), while maintaining all the advantages of CM-OTFS. For amplitude-clipped OTFS, the BER plateaus at a nonzero value, regardless of the SNR. As the amplifier-related distortion is not channel-dependent, it creates constant noise regardless of the channel conditions. When considering possible use cases of ISAC OTFS systems that involve high power transmission for radar operation, not achieving a good BER due to the amplitude clipping regardless of the high signal level is a substantial shortcoming with nonconstant modulus signals, such as OTFS. Instead, when CM-OTFS is used, good communication links could be established, as CM-OTFS enables high power transmission without distortion, helping to bridge the gap of required SNR.

To gain a better understanding of the role of CM-OTFS frame synthesis approach in the degradation of communications performance, the recovered symbol constellation for a high SNR iteration (SNR = 30 dB) is plotted in Fig. 11. This representation shows the spread of the symbols caused primarily by channel-unrelated effects. For clipped OTFS, we see a substantial increase in random noise-like error when compared to pristine OTFS, showing that the amplitude clipping appears similar to white Gaussian noise in the IQ plane. The stronger the distortion (the lower the IBO), the higher the symbols spread. The recovered CM-OTFS symbols display a similar level of spread in terms of magnitude to pristine OTFS but also show a considerable phase deviation caused by the cumulative phase error in the decoding process, resulting in reduced

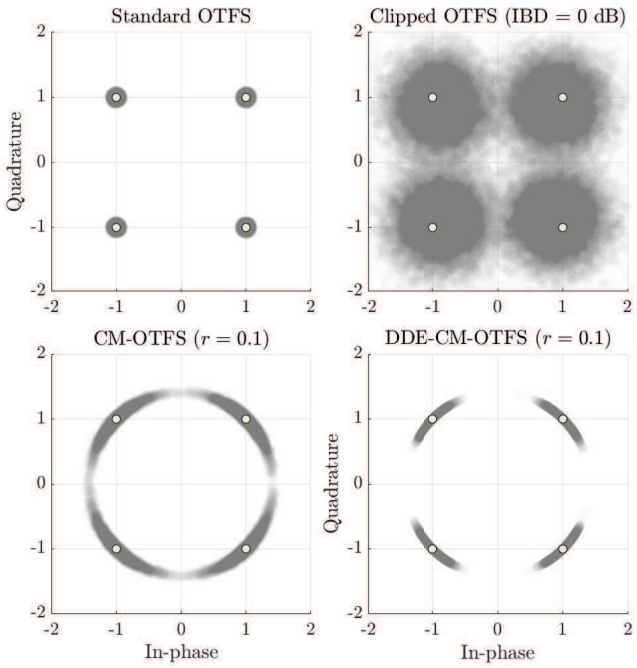

Fig. 11. Constellation of reconstructed symbols after channel compensation for SNR = 30 dB. Pristine OTFS on the top-left, amplifier distorted OTFS on the top-right, CM-OTFS on the bottom-left, and DDE-CM-OTFS on the bottom-right.

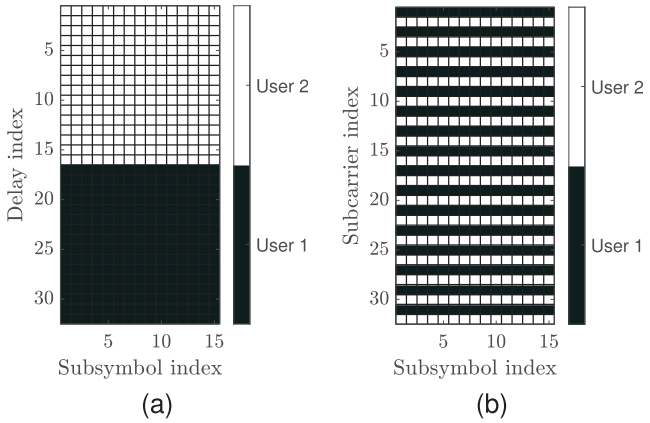

Fig. 12. Example of frequency division multiplexing (FDM) orthogonal multiple access for OTFS based on subcarrier interleaving. The stacking of the CM-OTFS signals in (a) results in an interleaving in the time–frequency domain in (b), making the signals separable in reception, and retaining the constant modulus property.

communications performance. It is observed in simulations that as the SNR increases, the phase error decreases until disappearing, resulting in the steadily decreasing BER value in Fig 10. The phase drift in the recovered symbols using DDE (DDE-CM-OTFS) is significantly reduced, resulting in considerable performance improvement compared to standard CM-OTFS.

Multiple access is also a crucial aspect when it comes to the usability of CM-OTFS in hybrid radar and communication scenarios. The ability to separate transmitters in MIMO radar and users in multiuser communications is crucial for both applications. The multiplexing of multiple transmitters/users for standard OTFS in orthogonal time–frequency patterns has been explored in [17] and [30]. The flexibility to use the same

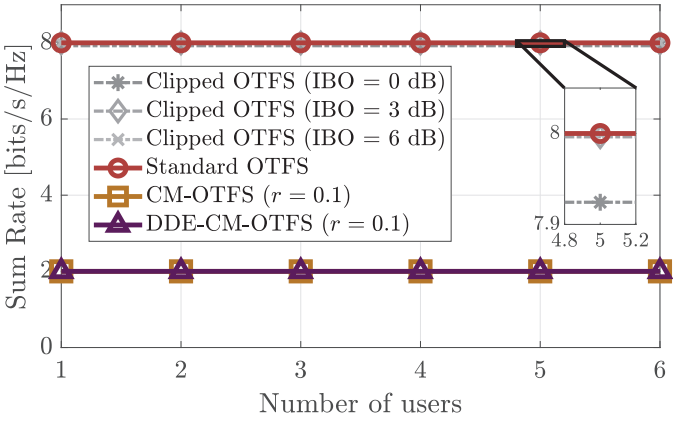

Fig. 13. Sum rate of QPSK OTFS and CM-OTFS with the proposed FDM OMA and SNR = 30 dB. The 4× rate reduction of CM-OTFS, and the scalability to multiple users can be observed.

Fig. 14. PARSAX (left) and measured industrial chimney at approximately 1185 m from the radar sensor (right).

time–frequency domain multiplexing is limited in the proposed Zak-transform-based OTFS, as the symbols are integrated together with the complementary sequences in the Doppler domain. However, multiplexing of multiple users/transmitters can be achieved in the delay/frequency domain, as the Zak transform does not affect that dimension. A representative example is shown in Fig. 12, where it is shown that a block-wise separation of users in the delay-subsymbol domain (after the Zak transform) results in nonoverlapping time–frequency representations. Moreover, the resulting time-domain signal retains the constant modulus properties that drive the proposed waveform synthesis approach. This approach for multiple access OTFS is discussed in depth in [30], where its performance is evaluated for different pulse properties and channel conditions. To test the compatibility of this approach with CM-OTFS, the same communication scenario as used for Figs. 10 and 11 is simulated with multiple users, whose signals are stacked in the delay domain, as in Fig. 12(a). The sum rate for an increasing amount of users is shown in Fig. 13, where we see that it remains constant regardless of the number of uses, due to the orthogonality between the waveforms. Additionally, the results clearly show the 4× reduction in sum rate due to the required redundancy in the CM-OTFS signal synthesis process mentioned in Section II. The results imply that the data rate of each user is limited by the total amount of shared bandwidth and time. To overcome this limitation, the combination of CM-OTFS with nonorthogonal multiple access methods, such as code and beamspace multiplexing, should be explored in future research.

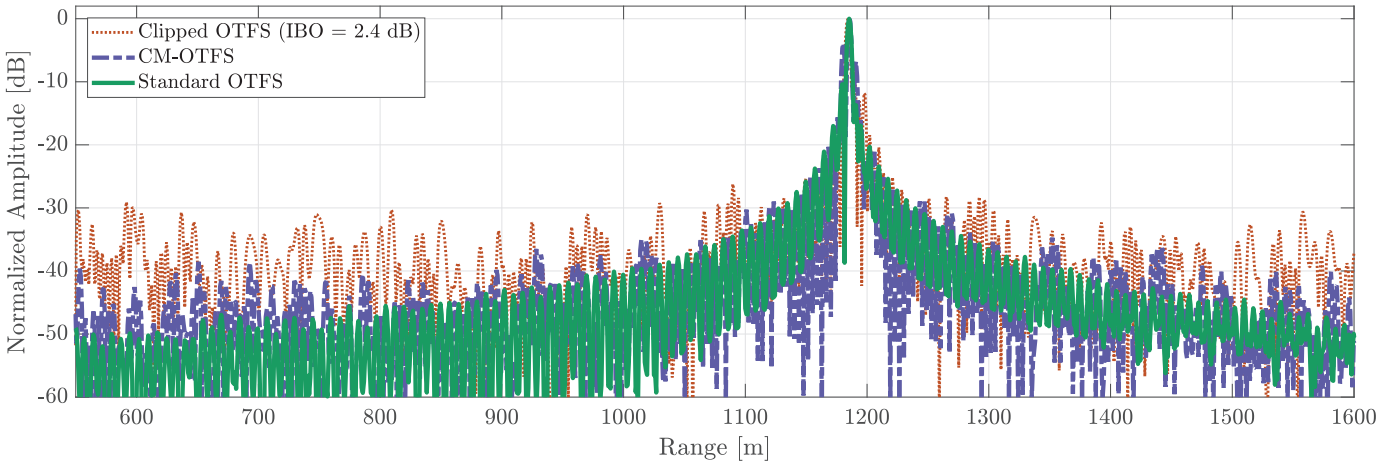

Fig. 15. Range cut of the range-Doppler radar estimation measured with PARSAX, without tapering. All estimations are normalized to their maximum and show a peak at the correct target position.

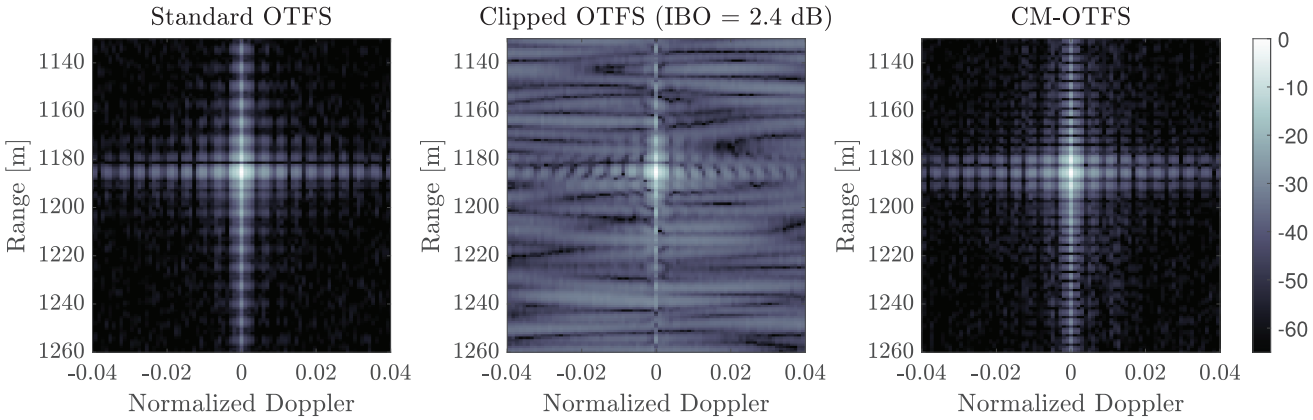

Fig. 16. Range-Doppler radar estimation measured with PARSAX, without tapering. Pristine OTFS on the left, OTFS with simulated amplifier distortion (IBO = 2.4 dB) on the center, and CM-OTFS on the right.

V. Experimental Validation of CM-OTFS Radar

In this section, the experimental results of CM-OTFS radar are presented and compared with standard OTFS radar with and without amplifier-related distortion. The data are acquired using the PARSAX radar [39] and a polarimetric waveform-agile radar used previously to validate MIMO nonuniform OTFS [40]. For the experiments in this work, a single polarimetric channel (HH) is used to measure a static target at 1185-m distance. The radar and the target are shown in Fig. 14. Three measurements are carried out: first, a standard OTFS frame is used without any amplifier-caused distortion; second, a signal with simulated amplifier-caused amplitude clipping IBO = 2.4 dB is used to measure the same target; finally, a measurement is carried out with the proposed CM-OTFS waveform ($r = 0.1$). The waveform parameters are shown in Table II are set, so that all waveforms share the same coherent processing time and bandwidth. The implication is that the CM-OTFS waveform transmits only a quarter of the communication symbols as the other two waveforms.

The zero-Doppler range cut for all three waveforms is shown in Fig. 15, where it can be seen that all three waveforms show a clear peak in the correct position of the target at 1185 m. It is also apparent that the standard undistorted OTFS waveform shows the best estimation, with the highest dynamic range. The CM-OTFS measurement shows slightly increased sidelobe levels, particularly far from the target position, but comparatively lower than the measurement with the distorted OTFS signal, represented by the orange dotted curve. CM-OTFS shows around 5–10-dB lower sidelobes than the measurement performed with an OTFS waveform suffering from simulated amplifier distortion. On the other hand, close side peaks appear in the range estimation next to the main peak of the CM-OTFS waveform, which aligns with the observation in the simulation of the degradation in radar performance of CM-OTFS compared to standard OTFS, affecting primarily the range cut. More observations can be

TABLE II
OTFS Experimental Waveform Parameters

Parameter	Symbol	Value
Number of delay bins	N	1024
Number of Doppler bins	M	812
Bandwidth	B	40 MHz
Carrier frequency	f_c	3.315 GHz
Symbol duration	T	25.6 μs
Intercarrier separation	Δf	39.06 kHz
Cyclic prefix duration	T_{cp}	12.8 μs
Communication Modulation	$(-)$	QPSK

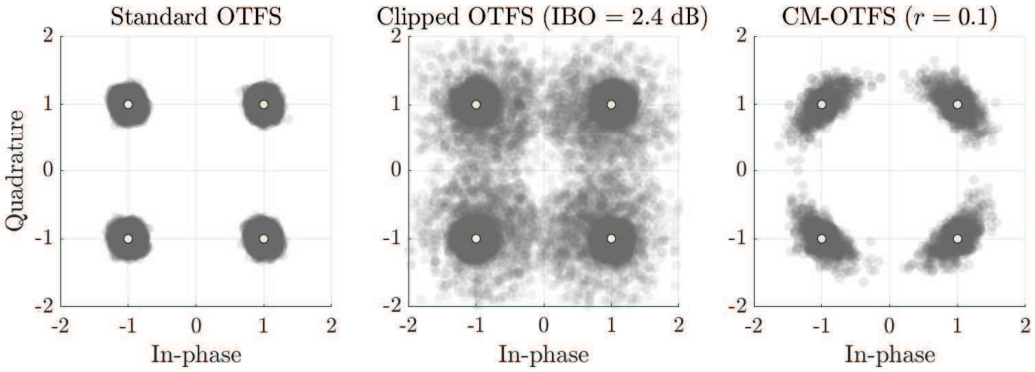

Fig. 17. Constellation of reconstructed symbols at the radar receiver. Channel compensation is performed using the monostatic radar estimation, assuming a single path.

made from Fig. 16, where the range-Doppler map around the target position is shown for all three waveforms. The standard OTFS measurement, on the left, shows the typical sync-like decreasing sidelobes in both range and Doppler. The clipped OTFS measurement shows a slightly increased range and Doppler sidelobes in the cells aligned with the target positions, but more importantly, it shows approximately 30-dB degradation in the bins not aligned with the correct range Doppler. This sort of degradation extends over the entire range-Doppler plane. It would significantly impair the estimation of multiple targets, particularly considering that there is no access to the distorted signal in the system that could otherwise be used to remove the sidelobes through model-based processing. The sidelobes in the CM-OTFS waveform are also steadily decreasing sinc-like sidelobes. Although they extend to the spurious peaks adjacent to the correct target position, they are confined to those specific range values and do not affect other areas of the range-Doppler plane.

In addition to the radar performance, we assess the communication functionality by recovering the delay-Doppler symbols embedded in the received radar waveform. The radar receive chain is repurposed as a communications receiver: the range-Doppler estimate obtained from the monostatic radar processing is treated as a single-path channel estimate, the dominant path corresponding to the chimney reflection. This estimate is then used to equalize the baseband signal and to decode the delay-Doppler symbols following the procedure of Section IV-B. The resulting symbol constellations are depicted in Fig. 17. As expected, pristine OTFS exhibits the tightest clustering. The clipped-OTFS case, which emulates amplifier saturation, shows a noticeable dispersion that would increase the probability of symbol errors at modest SNR. Crucially, the symbols conveyed with the proposed CM-OTFS waveform are successfully recovered after equalization, and their scatter matches the trend observed in the simulations.

These findings validate the end-to-end signal-processing chain proposed for CM-OTFS operation, confirming that both sensing and communications functions can be achieved without requiring separate hardware paths or calibration steps. The experiment therefore demonstrates the practical viability of CM-OTFS as a dual-function waveform under realistic front-end constraints. In fact, the experimental results with the clipped signal show more degradation than the degradation predicted in simulations, suggesting that abrupt amplitude clipping in the signal causes further hardware-related nonlinear effects than those modeled in our numerical simulations.

VI. Conclusion

A novel waveform, CM-OTFS, has been introduced in this article to address the problem of amplifier-related distortion in OTFS signals due to their nonconstant envelope property. It has been shown that the PAPR of traditional OTFS increases with the number of Doppler bins, leading to reduced radar and communication performance due to amplifier-induced distortion. CM-OTFS was proposed to address this issue. Inspired by a pre-existing OFDM technique, CM-OTFS employs complementary sequences and the Zak transform to generate a constant-envelope time-domain signal encoding delay-Doppler symbols. A full ISAC system concept for CM-OTFS has been proposed and validated through a combination of numerical simulations and experiments. Radar numerical and experimental data show that CM-OTFS performs slightly worse than pristine OTFS in target estimation but outperforms OTFS with amplifier distortion, with the gap widening as the signal distortion increases. However, this robustness comes at a tradeoff in communication throughput, specifically as a fourfold reduction in data rate. The noise tolerance of CM-OTFS was improved by using DDE, achieving BER performance close to that of pristine OTFS. Although further research is required to assess the compatibility of CM-OTFS with multiuser nonorthogonal multiple access MIMO ISAC system concepts, the results presented suggest that CM-OTFS is a valid alternative to standard OTFS for ISAC applications. In particular, it is well suited for systems where high-power operation and/or low-cost front-end components are required, or as a tool to enable high-power sensing modes in adaptive/cognitive ISAC systems with limited repercussions in communication performance.

Appendix A
Derivation of $\hat{z}_1$ and $\hat{z}_2$

Starting from the identities (21) and (22) for the received signal, we have the system of equations

$$\hat{\mathbf{s}}_1 = \hat{\mathbf{z}}_1 + je^{j\phi_c}\hat{\mathbf{z}}_2 \tag{49}$$

$$\hat{\mathbf{s}}_2 = \hat{\mathbf{z}}_1 - je^{j\phi_c}\hat{\mathbf{z}}_2 \tag{50}$$

where solving for $\hat{z}_1$ and $\hat{z}_2$, we can write

$$\hat{\mathbf{z}}_1 = \hat{\mathbf{s}}_1 - je^{j\phi_c}\hat{\mathbf{z}}_2 \tag{51}$$

$$\hat{\mathbf{z}}_2 = -\frac{\hat{\mathbf{s}}_2 - \hat{\mathbf{z}}_1}{j}e^{-j\boldsymbol{\phi}_c}. \tag{52}$$

By substituting $\hat{z}_1$ from (51) into (52), we get

$$\hat{\mathbf{z}}_2 = e^{-j\boldsymbol{\phi}_c}\frac{\hat{\mathbf{s}}_1 - \hat{\mathbf{s}}_2}{2j}. \tag{53}$$

Now, substituting $\hat{\mathbf{z}}_2$ from (53) into (51), the final expression for $\hat{\mathbf{z}}_1$ is

$$\hat{\mathbf{z}}_1 = \frac{\hat{\mathbf{s}}_1 + \hat{\mathbf{s}}_2}{2}. \tag{54}$$

thus arriving at the expressions for $\hat{\mathbf{z}}_1$ and $\hat{\mathbf{z}}_2$ used in (26) and (27).

APPENDIX B
DERIVATION OF $\hat{a}_m$

This appendix derives the expression for estimating the symbol $\hat{a}_m$ from the complementary sequences. For this appendix, and for compactness, the subscript in $\hat{a}_n$ denotes the nth element of $\hat{\mathbf{a}}$, whereas $\mathbf{c}_1$ and $\mathbf{c}_2$ denote two different vectors. This appendix follows the steps given in [41] with the adapted notation to fit CM-OTFS. The starting Golay sequences are initialized as

$$\mathbf{c}_1^{(-1)}[n] = \{1, 1\}, \mathbf{c}_2^{(-1)}[n] = \{1, -1\}$$

which after the first inner iteration of Algorithm 1, becomes

$$\mathbf{c}_1^{(0)} = \{a_0, a_0 - r, r\} \tag{55}$$

$$\mathbf{c}_2^{(0)} = \left\{x, a_0^* + r, -a_0^*\right\}. \tag{56}$$

And after the second next iteration

$$\mathbf{c}_1^{(1)} = \left\{a_1a_0, a_1a_0 - ra_1 - r^2, a_1r - ra_0^* - r^2, r\ a_0^*\right\} \tag{57}$$

$$\mathbf{c}_2^{(1)} = \left\{ra_0, r\ a_0^* + r^2, -a_1^*a_0^* + ra_1^* + r^2, -a_1^*a_0^*\right\}. \tag{58}$$

To isolate a_1, we select the second and penultimate elements of $\mathbf{c}_1^{(1)}$ and $\mathbf{c}_2^{(1)}$, and we can get an estimate of a_1 as

$$\hat{a}_1 = r\frac{c_1^{(1)}[1] + c_2^{(1)}[2]^*}{c_2^{(1)}[1] - c_1^{(1)}[2]^*}. \tag{59}$$

More generally, from (14), and again for the second and penultimate entries of $\mathbf{c}_1^{(m)}$ and $\mathbf{c}_2^{(m)}$ at the mth iteration (N_m being the last sample of the sequences), we can write

$$c_1^{(m)}[1] = a_m c_1^{(m-1)}[1] + rc_2^{(m-1)}[0] \tag{60}$$

$$c_2^{(m)}[1] = -rc_1^{(m-1)}[1] + a_m^* c_2^{(m-1)}[0] \tag{61}$$

$$c_1^{(m)}[N_m - 1] = a_m c_1^{(m-1)}[N_m - 1] + rc_2^{(m)}[N_m - 1] \tag{62}$$

$$c_2^{(m)}[N_m - 1] = -rc_1^{(m-1)}[N_m - 1] + a_m^* c_2^{(m)}[N_m - 1]. \tag{63}$$

Since $c_1^{(k)}[0] = -c_2^{(k)}[N_k]^*$ and $c_1^{(k)}[N_k] = c_2^{(k)}[0]^*$ for all k, the extraneous terms will continue to cancel. Therefore, by induction on (59)

$$\hat{a}_m = r\frac{c_1^{(m)}[1] + c_2^{(m)}[N_m - 1]^*}{c_2^{(m)}[1] - c_1^{(m)}[N_m - 1]^*} \tag{64}$$

for any $m \geq 1$.

ACKNOWLEDGMENT

The authors thank Fred van der Zwan for his support during the measurement campaigns.

REFERENCES

[1] K. V. Mishra, M. R. Bhavani Shankar, V. Koivunen, B. Ottersten, and S. A. Vorobyov, "Toward millimeter-wave joint radar communications: A signal processing perspective," *IEEE Signal Process. Mag.*, vol. 36, no. 5, pp. 100–114, Sep. 2019.

[2] A. Hassanien, M. G. Amin, Y. D. Zhang, and F. Ahmad, "Dual-function radar-communications: Information embedding using sidelobe control and waveform diversity," *IEEE Trans. Signal Process.*, vol. 64, no. 8, pp. 2168–2181, Apr. 2016.

[3] F. Liu, C. Masouros, A. Li, H. Sun, and L. Hanzo, "MU-MIMO communications with MIMO radar: From co-existence to joint transmission," *IEEE Trans. Wireless Commun.*, vol. 17, no. 4, pp. 2755–2770, Apr. 2018.

[4] J. Xu, X. Wang, E. Aboutanios, and G. Cui, "Hybrid index modulation for dual-functional radar communications systems," *IEEE Trans. Veh. Technol.*, vol. 72, no. 3, pp. 3186–3200, Mar. 2023.

[5] P. Kumari, J. Choi, N. González-Prelcic, and R. W. Heath, "IEEE 802.11ad-based radar: An approach to joint vehicular communication-radar system," *IEEE Trans. Veh. Technol.*, vol. 67, no. 4, pp. 3012–3027, Apr. 2018.

[6] B. Schweizer et al., "The fairy tale of simple all-digital radars: How to deal with 100 Gbit/s of a digital millimeter-wave MIMO radar on an FPGA [Application Notes]," *IEEE Microw. Mag.*, vol. 22, no. 7, pp. 66–76, Jul. 2021.

[7] C. Sturm, E. Pancera, T. Zwick, and W. Wiesbeck, "A novel approach to OFDM radar processing," in *Proc. IEEE Radar Conf.*, Pasadena, CA, USA, May 2009, pp. 1–4.

[8] C. Sturm and W. Wiesbeck, "Waveform design and signal processing aspects for fusion of wireless communications and radar sensing," *Proc. IEEE*, vol. 99, no. 7, pp. 1236–1259, Jul. 2011.

[9] M. F. Keskin, H. Wymeersch, and V. Koivunen, "MIMO-OFDM joint radar-communications: Is ICI friend or foe?," *IEEE J. Sel. Topics Signal Process.*, vol. 15, no. 6, pp. 1393–1408, Nov. 2021.

[10] R. Hadani and A. Monk, "OTFS: A new generation of modulation addressing the challenges of 5G," 2018, *arXiv:1802.02623*.

[11] A. Correas-Serrano, N. Petrov, M. Gonzalez-Huici, and A. Yarovoy, "Emerging trends in radar: OTFS-based radar for integrated sensing and communications systems," *IEEE Aerosp. Electron. Syst. Mag.*, vol. 40, no. 6, pp. 102–107, Jun. 2025.

[12] L. Gaudio, G. Colavolpe, and G. Caire, "OTFS vs. OFDM in the presence of sparsity: A fair comparison," *IEEE Trans. Wireless Commun.*, vol. 21, no. 6, pp. 4410–4423, Jun. 2022.

[13] P. Raviteja, Y. Hong, E. Viterbo, and E. Biglieri, "Practical pulse-shaping waveforms for reduced-cyclic-prefix OTFS," *IEEE Trans. Veh. Technol.*, vol. 68, no. 1, pp. 957–961, Jan. 2019.

[14] P. Raviteja, K. T. Phan, Y. Hong, and E. Viterbo, "Orthogonal time frequency space (OTFS) modulation based radar system," in *Proc. IEEE Radar Conf. (RadarConf)*, Apr. 2019, pp. 1–6.

[15] L. Gaudio, M. Kobayashi, G. Caire, and G. Colavolpe, "On the effectiveness of OTFS for joint radar parameter estimation and communication," *IEEE Trans. Wireless Commun.*, vol. 19, no. 9, pp. 5951–5965, Sep. 2020.

[16] A. Correas-Serrano, N. Petrov, M. Gonzalez-Huici, and A. Yarovoy, "Comparison of radar receivers for OFDM and OTFS waveforms," in *Proc. 19th Eur. Radar Conf. (EuRAD)*, Sep. 2022, pp. 1–4.

[17] A. Correas-Serrano, N. Petrov, M. Gonzalez-Huici, and A. Yarovoy, "MIMO OTFS with arbitrary time-frequency allocation for joint radar and communications," *IEEE Trans. Radar Syst.*, vol. 1, pp. 707–718, 2023.

[18] A. Correas-Serrano, N. Petrov, M. Gonzalez-Huici, and A. Yarovoy, "Optimized time-frequency allocation in MIMO NU-OTFS radar for enhanced performance under spectral constraints," in *Proc. IEEE Radar Conf. (RadarConf24)*, May 2024, pp. 1–6.

[19] M. F. Keskin, C. Marcus, O. Eriksson, A. Alvarado, J. Widmer, and H. Wymeersch, "Integrated sensing and communications with MIMO-OTFS: ISI/ICI exploitation and Delay-Doppler multiplexing," *IEEE Trans. Wireless Commun.*, vol. 23, no. 8, pp. 10229–10246, Aug. 2024.

[20] S. K. Dehkordi, L. Gaudio, M. Kobayashi, G. Caire, and G. Colavolpe, "Beam-space MIMO radar for joint communication and sensing with OTFS modulation," *IEEE Trans. Wireless Commun.*, vol. 22, no. 10, pp. 6737–6749, Oct. 2023.

[21] G. D. Surabhi, R. M. Augustine, and A. Chockalingam, "Peak-to-Average power ratio of OTFS modulation," *IEEE Commun. Lett.*, vol. 23, no. 6, pp. 999–1002, Jun. 2019.

[22] D. Guel and J. Palicot, "Analysis and comparison of clipping techniques for OFDM peak-to-average power ratio reduction," in *Proc. 16th Int. Conf. Digit. Signal Process.*, Jul. 2009, pp. 1–6.

[23] S. Chang, E. J. Powers, and J. Chung, "A compensation scheme for nonlinear distortion in OFDM systems," in *Proc. IEEE Global Telecommun. Conf. Rec.*, vol. 2, Apr. 2000, pp. 736–740.

[24] B. D. Carlton and J. G. Metcalf, "Orthogonal frequency peak-to-average power ratio reduction via the error reduction algorithm," in *Proc. IEEE Radar Conf.*, Mar. 2022, pp. 1–6.

[25] P. Varshney, P. Babu, and P. Stoica, "Low-PAPR OFDM waveform design for radar and communication systems," *IEEE Trans. Radar Syst.*, vol. 1, pp. 69–74, 2023.

[26] S. C. Thompson, A. U. Ahmed, J. G. Proakis, J. R. Zeidler, and M. J. Geile, "Constant envelope OFDM," *IEEE Trans. Commun.*, vol. 56, no. 8, pp. 1300–1312, Aug. 2008.

[27] K. Willstatter and M. D. Zoltowski, "Complementary sequence encoding for 1D and 2D constant-modulus OFDM transmission at millimeter wave frequencies," in *Proc. IEEE Int. Conf. Acoust., Speech Signal Process. (ICASSP)*, May 2019, pp. 4804–4808.

[28] K. Willstatter and M. D. Zoltowski, "Complementary sequence construction for constant-envelope OFDM transmission enabling nonlinear amplification and clipping," in *Proc. IEEE Mil. Commun. Conf. (MILCOM)*, Nov. 2021, pp. 390–395.

[29] S. P. Lavery and T. Ratnarajah, "Remote sensing with constant-modulus OFDM signals from complementary sequences," in *Proc. IEEE Radar Conf.*, May 2024, pp. 1–6.

[30] V. Khammammetti and S. Khan Mohammed, "Spectral efficiency of OTFS based orthogonal multiple access with rectangular pulses," 2021, *arXiv:2110.08746*.

[31] M. C. Jeruchim, P. Balaban, and K. S. Shanmugan, *Simulation of Communication Systems: Modeling, Methodology and Techniques*. Cham, Switzerland: Springer, 2006.

[32] E. Costa, M. Midrio, and S. Pupolin, "Impact of amplifier nonlinearities on OFDM transmission system performance," *IEEE Commun. Lett.*, vol. 3, no. 2, pp. 37–39, Feb. 1999.

[33] H. Ochiai, "Performance analysis of peak power and band-limited ofdm system with linear scaling," *IEEE Trans. Wireless Commun.*, vol. 2, no. 5, pp. 1055–1065, Sep. 2003.

[34] K. Willstatter, "Constant-modulus OFDM transmission using complementary sequences," Ph.D. dissertation, Purdue Univ. Graduate School, West Lafayette, IN, USA, Dec. 2022, doi: 10.25394/PGS.21669644.v1.

[35] M. Bica and V. Koivunen, "Generalized multicarrier radar: Models and performance," *IEEE Trans. Signal Process.*, vol. 64, no. 17, pp. 4389–4402, Sep. 2016.

[36] Z. Cui, P. Zhang, and S. Pollin, "6G wireless communications in 7–24 GHz band: Opportunities, techniques, and challenges," 2023, *arXiv:2310.06425*.

[37] M.-E. Chatzitheodoridi, A. Taylor, and O. Rabaste, "A mismatched filter for integrated sidelobe level minimization over a continuous Doppler shift interval," in *Proc. IEEE Radar Conf.*, Sep. 2020, pp. 1–6. [Online]. Available: https://hal.archives-ouvertes.fr/hal-03104178

[38] Y. Hong, T. Thaj, and E. Viterbo, *Delay-Doppler Communications: Principles and Applications*. Amsterdam, The Netherlands: Elsevier, 2022.

[39] O. A. Krasnov, G. P. Babur, Z. Wang, L. P. Ligthart, and F. van der Zwan, "Basics and first experiments demonstrating isolation improvements in the agile polarimetric FM-CW radar–PARSAX," *Int. J. Microw. Wireless Technol.*, vol. 2, nos. 3–4, pp. 419–428, Aug. 2010.

[40] A. Correas-Serrano, N. Petrov, M. Gonzalez-Huici, and A. Yarovoy, "Experimental validation of NU-OTFS MIMO radar through polarimetric measurements," in *Proc. 21st Eur. Radar Conf. (EuRAD)*, Sep. 2024, pp. 63–66.

[41] K. Willstatter. (2022). *Constant-Modulus OFDM Transmission Using Complementary Sequences*. [Online]. Available: https://hammer.purdue.edu/articles/thesis/Constant-ModulusOFDMTransmissionUsingComplementarySequences/21669644

Aitor Correas-Serrano received the B.Sc. and M.Sc. degrees in telecommunications engineering from the Technical University of Cartagena, Spain, in 2015 and 2017, respectively. He began pursuing a Ph.D. degree with the Microwave Sensing, Signals and Systems Group, Delft University of Technology (TU Delft), Delft, The Netherlands, in January 2020.

During his master's studies, he joined the Fraunhofer Institute for High Frequency Physics and Radar Techniques (FHR), Wachtberg, Germany, as a Research Engineer, focusing on compressed sensing methods for automotive radar. Since 2017, he has been a Research Associate with Fraunhofer FHR, where he works on advanced radar technologies. His research interests include compressed sensing, MIMO waveform design, interference mitigation, and adaptive strategies for multifunctional radar-communication systems.

Dr. Correas-Serrano has served as a reviewer for the IEEE TRANSACTIONS ON RADAR SYSTEMS, IEEE TRANSACTIONS ON VEHICULAR TECHNOLOGY, IEEE TRANSACTIONS ON AEROSPACE AND ELECTRONIC SYSTEMS, IEEE WIRELESS COMMUNICATIONS LETTERS, and several IEEE radar-related conferences.

Nikita Petrov received the Engineering degree in radio-electronic control systems from Baltic State Technical University Voenmeh, Saint Petersburg, Russia, in 2012, and the Ph.D. degree in radar signal processing from Delft University of Technology, Delft, The Netherlands, in 2019.

Since 2019, he has been a Post-Doctoral Researcher with the Microwave Sensing, Signals and Systems (MS3) Section, Faculty of Electrical Engineering, Mathematics, and Computer Science (EEMCS), Delft University of Technology. Since April 2022, he has been a Principal Radar Signal Processing Engineer at NXP Semiconductors N.V., Eindhoven, The Netherlands, and he holds an advisory position in the same group at Delft University of Technology. His research interests include modern radar technologies, radar signal processing, multichannel and multiband signals and systems, and high-resolution and automotive radars

Dr. Petrov serves as a Reviewer for a few IEEE Transactions and Radar Conferences.

Maria A. Gonzalez-Huici received the diploma degree in theoretical physics from the Autonoma University of Madrid, Madrid, Spain, in September 2002, the master's degree in particle physics and astrophysics from the University of Bonn, Bonn, Germany, and the Ph.D. degree in physics from the University of Bonn, in 2013, on the topic of detection and classification of buried landmines with radar.

Since May 2005, she has been working as a Research Associate at Fraunhofer FHR. Since 2015, she has been leading the Adaptive Perception team at FHR. Since April 2023, she has also been leading Signal Processing and Algorithms Department. Her research focuses on MIMO radar, signal and array processing, waveform design, compressed sensing, deep learning, and sensor data fusion.

Alexander Yarovoy (Fellow, IEEE) received the diploma degree (Hons.) in radiophysics and electronics and the Physics and Mathematics Science and Doctor Physics and Mathematics Science degrees in radiophysics from the Kharkov State University, Kharkiv, Ukraine, in 1984, 1987, and 1994, respectively.

In 1987, he joined the Department of Radiophysics, Kharkov State University, as a Researcher and became a Full Professor in 1997. From September 1994 to 1996, he was with the Technical University of Ilmenau, Germany, as a Visiting Researcher. Since 1999, he has been with Delft University of Technology, the Netherlands. Since 2009 he has been leads there a Chair of Microwave Sensing, Systems and Signals. He has authored and co-authored more than 550 scientific or technical papers, seven patents and fourteen book chapters. His main research interests are in high-resolution radar, microwave imaging and applied electromagnetics (in particular, UWB antennas).

Dr. Yarovoy is the recipient of the European Microwave Week Radar Award for the paper that best advances the state-of-the-art in radar technology in 2001 (together with L.P. Ligthart and P. van Genderen) and in 2012 (together with T. Savelyev). In 2023 together with Dr. I.Ullmann, N. Kruse, R. Gündel and Dr. F. Fioranelli he got the best paper award at IEEE Sensor Conference. In 2010 together with D. Caratelli he got the best paper award of the Applied Computational Electromagnetic Society (ACES). He served as the General TPC chair of the 2020 European Microwave Week (EuMW'20), as the Chair and TPC chair of the 5th European Radar Conference (EuRAD'08), as well as the Secretary of the 1st European Radar Conference (EuRAD'04). He served also as the co-chair and TPC chair of the Xth International Conference on GPR (GPR2004). He serves as an Associated Editor of the IEEE TRANSACTION ON RADAR SYSTEMS. From 2011 to 2018, he served as an Associated Editor of the *International Journal of Microwave and Wireless Technologies*. In the period 2008 to 2017, he served as the Director of the European Microwave Association (EuMA).